doi:10.1038/nature19060

Enhanced electrocatalytic CO_2 reduction via field-induced reagent concentration

Min Liu[1]*, Yuanjie Pang[2]*, Bo Zhang[1,3]*, Phil De Luna[4]*, Oleksandr Voznyy[1], Jixian Xu[1], Xueli Zheng[1,5], Cao Thang Dinh[1], Fengjia Fan[1], Changhong Cao[2], F. Pelayo García de Arquer[1], Tina Saberi Safaei[1], Adam Mepham[6], Anna Klinkova[7], Eugenia Kumacheva[7], Tobin Filleter[2], David Sinton[2], Shana O. Kelley[6,8,9] & Edward H. Sargent[1]

Electrochemical reduction of carbon dioxide (CO_2) to carbon monoxide (CO) is the first step in the synthesis of more complex carbon-based fuels and feedstocks using renewable electricity[1–7]. Unfortunately, the reaction suffers from slow kinetics[7,8] owing to the low local concentration of CO_2 surrounding typical CO_2 reduction reaction catalysts. Alkali metal cations are known to overcome this limitation through non-covalent interactions with adsorbed reagent species[9,10], but the effect is restricted by the solubility of relevant salts. Large applied electrode potentials can also enhance CO_2 adsorption[11], but this comes at the cost of increased hydrogen (H_2) evolution. Here we report that nanostructured electrodes produce, at low applied overpotentials, local high electric fields that concentrate electrolyte cations, which in turn leads to a high local concentration of CO_2 close to the active CO_2 reduction reaction surface. Simulations reveal tenfold higher electric fields associated with metallic nanometre-sized tips compared to quasi-planar electrode regions, and measurements using gold nanoneedles confirm a field-induced reagent concentration that enables the CO_2 reduction reaction to proceed with a geometric current density for CO of 22 milliamperes per square centimetre at −0.35 volts (overpotential of 0.24 volts). This performance surpasses by an order of magnitude the performance of the best gold nanorods, nanoparticles and oxide-derived noble metal catalysts. Similarly designed palladium nanoneedle electrocatalysts produce formate with a Faradaic efficiency of more than 90 per cent and an unprecedented geometric current density for formate of 10 milliamperes per square centimetre at −0.2 volts, demonstrating the wider applicability of the field-induced reagent concentration concept.

The Gibbs free energy (ΔG) diagrams obtained from density functional theory (DFT) calculations on gold (Au) surface models of various facets at 298 K, 1 atm and 0 V versus reversible hydrogen electrode (RHE) are given in Fig. 1 (see also Extended Data Fig. 1 and Extended Data Table 1a–c), showing that adsorbed K^+ ions lower the thermodynamic energy barrier for reaction for all facets. On the Au(111) gold surface, the adsorbed K^+ stabilizes the COOH* and CO* intermediates by 0.89 eV and 0.24 eV, respectively (Fig. 1a). On Au(100) and Au(110), it stabilizes the rate-determining COOH* intermediate[8] by 0.66 eV and 0.69 eV, respectively (Fig. 1b, c). On the under-coordinated Au(211) facet, K^+ similarly stabilizes COOH* and CO* (Fig. 1d). We further note that in the presence of adsorbed K^+, a greater electron density is found on the carbon of the COOH*

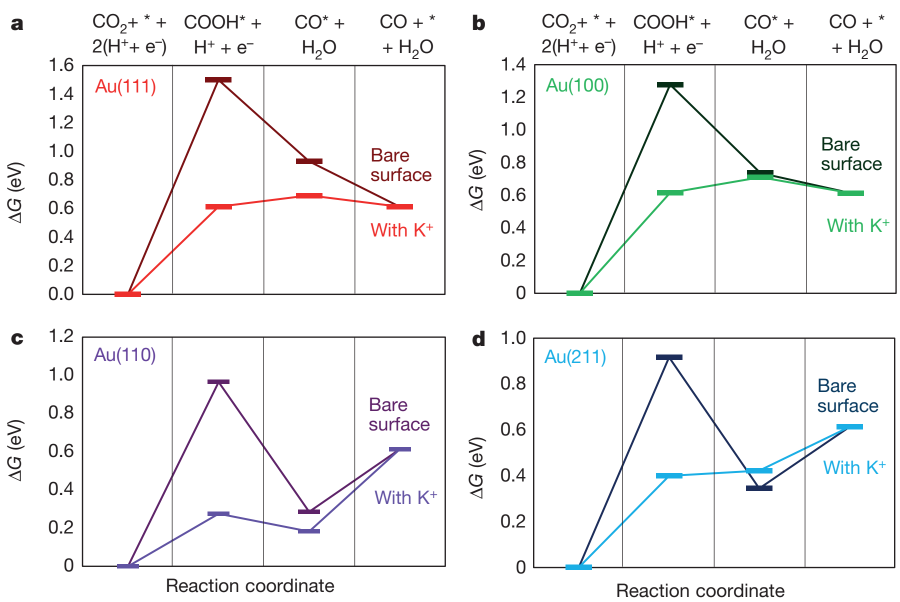

Figure 1 | Thermodynamic barriers for the CO_2-to-CO reduction reaction on Au surface under conditions with and without K^+. Gibbs free energy ΔG diagrams of the electrochemical reduction of CO_2 to CO on Au(111) (**a**), Au(100) (**b**), Au(110) (**c**) and Au(211) (**d**) facets in the presence of adsorbed K^+ and in the absence of adsorbed K^+.

[1]Department of Electrical and Computer Engineering, University of Toronto, 35 St George Street, Toronto, Ontario M5S 1A4, Canada. [2]Department of Mechanical and Industrial Engineering, University of Toronto, 5 King's College Road, Toronto, Ontario M5S 3G8, Canada. [3]Department of Physics, East China University of Science and Technology, 130 Meilong Road, Shanghai 200237, China. [4]Department of Materials Science and Engineering, University of Toronto, 184 College Street, Toronto, Ontario M5S 3E4, Canada. [5]Tianjin Key Laboratory of Composite and Functional Materials, School of Materials Science and Engineering, Tianjin University, Tianjin 300072, China. [6]Institute of Biomaterials and Biomedical Engineering, University of Toronto, 164 College Street, Toronto, Ontario M5S 3G9, Canada. [7]Department of Chemistry, University of Toronto, 80 St George Street, Toronto, Ontario M5S 3H6, Canada. [8]Department of Pharmaceutical Sciences, Leslie Dan Faculty of Pharmacy, University of Toronto, 144 College Street, Toronto, Ontario M5S 3M2, Canada. [9]Department of Biochemistry, University of Toronto, 1 King's College Circle, Toronto, Ontario M5S 1A8, Canada.
*These authors contributed equally to this work.

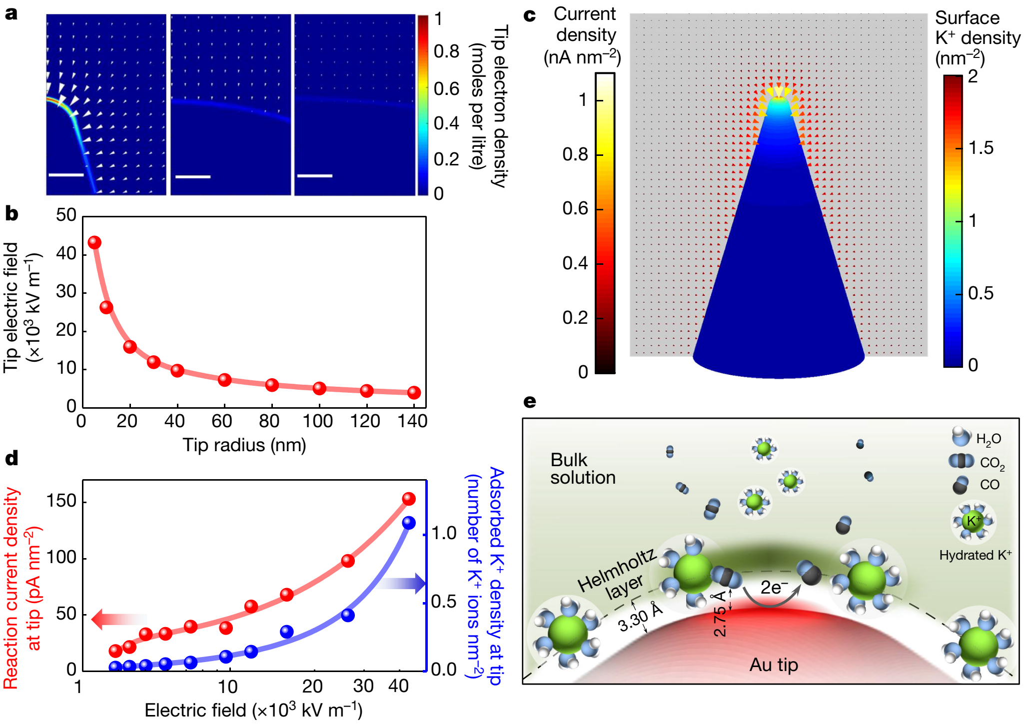

Figure 2 | Computed electric field, K^+ concentration and current density near the tip of an electrode as a function of tip radius. a, Free electron density distribution on the surface of electrodes is shown as a colour map. Electrostatic field distribution around the electrode is shown as a group of arrows, where the size and direction of each arrow represent the magnitude and direction of the field at the arrow's spatial position. The tip radius of the structure in each panel is 5 nm (left), 60 nm (middle) and 140 nm (right). Scale bars represent 5 nm. **b**, Electrostatic field intensity at the electrode tip increases as the tip radius decreases. **c**, Surface K^+ density and current density distributions on the surface of Au needles. The tip radius is 5 nm. **d**, Adsorbed K^+ and reaction current density as functions of the electric field intensity at the tip. **e**, A schematic showing how K^+ ions on the gold surface help CO_2 molecule adsorption.

intermediate, suggesting a stronger C–Au bond (Extended Data Fig. 1e) and further indicating that adsorbed cations modulate the CO_2 reduction reaction.

Ab initio molecular dynamics simulations reveal that the presence of K^+ reduces the mean square displacement of CO_2 relative to the surface by a factor of 2.3, compared to the system with no K^+ (Extended Data Fig. 1f), converging to approximately 2.5 Å^2 regardless of facet (Extended Data Fig. 1g). The nearest-neighbour C–Au distances obtained from simulated radial distribution function peaks are 2.75 Å and 3.25 Å in the presence and absence of K^+, respectively (Extended Data Fig. 1h and Extended Data Table 1d). Further, the interaction energy of CO_2 on the Au surface with K^+ is consistently smaller (Extended Data Fig. 1i).

These results suggest that locally concentrating cations at reactive sites could enhance CO_2 electroreduction. As high-curvature structures are known to concentrate electric fields that can affect ion concentrations, we used a finite-element numerical method to explore the prospects of tip-enhanced nanometre-scale field intensification and cation concentration. Cones with rounded tips were used to represent sharp electrode tips immersed in an electrolyte, with their tip-concentrated electron density (Fig. 2a) increasing as the electrodes sharpen. The locally enhanced electrostatic field is generated by, and points to, the locally concentrated free electron density on the surface of the electrodes (arrows in Fig. 2a). It originates from the migration of free electrons to the regions of the sharpest curvature on a charged metallic electrode, a consequence of electrostatic repulsion[12]. Tip sharpening from a radius of 140 nm to 5 nm enhances electrostatic field intensity (Fig. 2b) at the tip of the electrode, at the CO_2/CO equilibrium potential (−0.11 V), by one order of magnitude.

To estimate the quantitative impact of the electric field on the surface-adsorbed cation concentration, we used a Gouy–Chapman–Stern model (Extended Data Fig. 2a and Methods) to map the surface-adsorbed K^+ ion density in the Helmholtz layer of the electrical double layer directly adjacent to the electrode surface (Fig. 2c). This indicates a 20-fold increased surface-adsorbed K^+ ion concentration at the Au needle tip due to locally enhanced electrostatic field (Fig. 2d), while a sixfold increase in the bulk K^+ concentration in the electrolyte only doubles the field-induced K^+ ion concentration near the electrode (Extended Data Fig. 2b). Furthermore, increasing the applied cathode potential tenfold, from −0.11 V to −1.1 V (where the CO_2 reduction reaction—CO_2RR—is no longer selective because it competes against H_2 evolution) only doubles the field-induced K^+ ion concentration (Extended Data Fig. 2c). With concentrated K^+, CO_2 quickly (in 0.5 ps) stabilizes on the Au sharp features (Extended Data Fig. 2d) and CO_2RR mostly occurs at the Au tips (Fig. 2c and Extended Data Fig. 2e), with the effect projected to increase the reduction current by two orders of magnitude (Fig. 2d). These results, taken together, point to field-induced reagent concentration (FIRC) as a means of enhancing CO_2RR appreciably (Fig. 2e).

To probe experimentally the predictions, we used electrodeposition as a convenient and scalable means of preparing desired electrodes[13] with a suite of tip radii (Fig. 3 and Extended Data Fig. 3a) ranging from large-diameter particles (radius of curvature of about 140 nm) to intermediate-diameter rods (radius of curvature of about 60 nm) to high-curvature nanoneedles (radius of curvature of about 5 nm). Electrochemical roughness factors were measured via two electrochemical methods[9,14], providing the values of 52, 33 and 12 for Au needle, rod and particle electrodes, respectively (Extended Data Fig. 3b, c and Extended Data Table 2). X-ray diffraction confirms that all micro- and nano-structures comprise a regular (uncompressed) gold lattice (Extended Data Fig. 3d). X-ray photoelectron spectroscopy and O K-edge X-ray absorption spectra show features characteristic of Au^0 and none attributable to oxide (Extended Data Figs 3d and 4a, b). High-resolution transmission electron microscopy (TEM) and the corresponding local electron energy loss spectroscopy (EELS, Extended Data Fig. 4c, d) show no Au adatoms or local Au oxide on the tips of the Au needles.

Kelvin probe atomic force microscopy confirmed that electric fields are highest for the needles and lowest for large particles (Fig. 3c, g, k). Secondary Au nanoparticle electrodeposition preferentially occurs at the tip of Au needles (Fig. 3d), decreases on Au rods and almost disappears on Au particles (Extended Data Fig. 5f). Au needles have the largest electric-field-induced locally absorbed K^+ concentration under performance-testing conditions (Fig. 3h), with conductive atomic force microscopy proving that the nanoscale local current at Au needle tips is higher than the current on Au rods and particles (Fig. 3l and Extended Data Fig. 2f). These results all support the

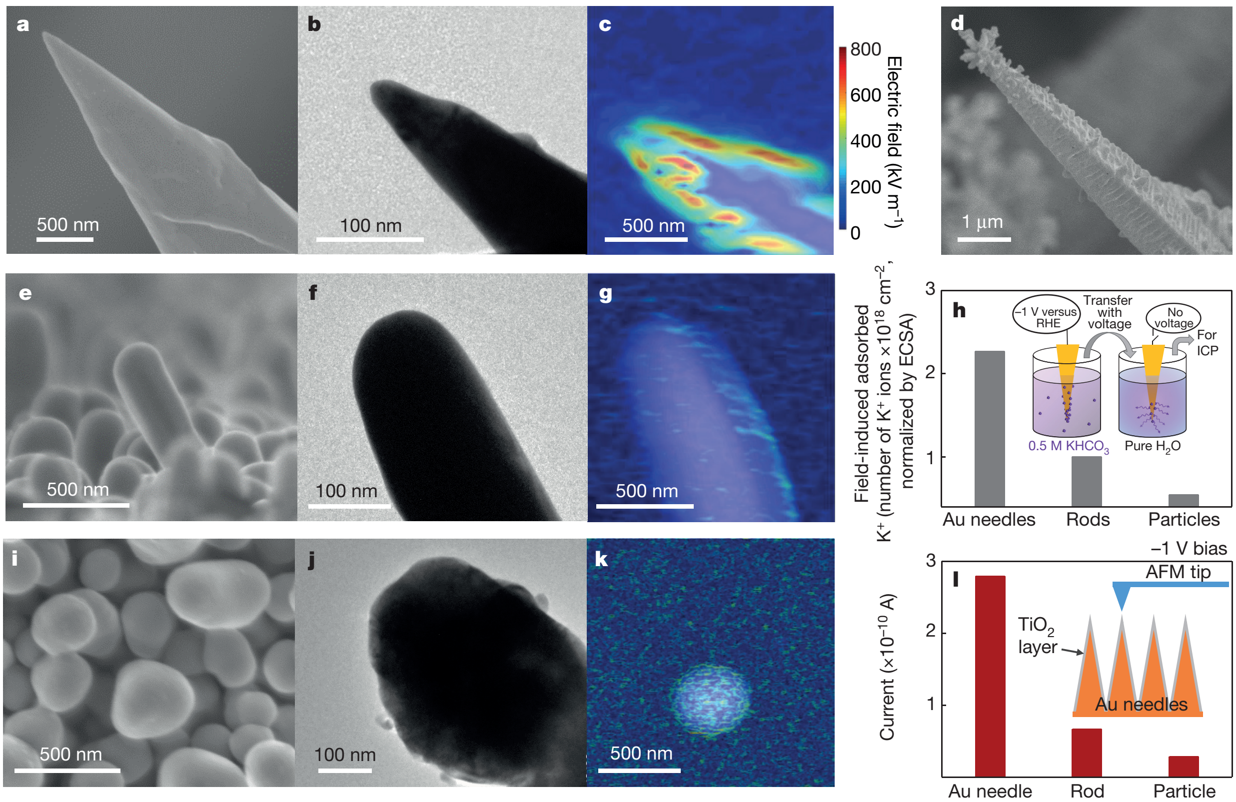

Figure 3 | Physical characterization of Au tips, rods and particles. **a**, **e**, **i**, Scanning electron microscopy (SEM) images; **b**, **f**, **j**, TEM images; **c**, **g**, **k**, Electric field distribution of Au needles, rods and particles deduced using Kelvin probe atomic force microscopy. **d**, SEM image of Au needle with secondarily deposited Au particles. **h**, ECSA-normalized field-induced concentration of adsorbed K^+ on Au needles, rods and particles. The concentration of K^+ was measured via inductively coupled plasma (ICP) optical emission spectrometry. The inset shows the process of measuring the field-induced adsorbed K^+. **l**, Current on a single Au needle, rod and particle with a thin TiO_2 insulator layer at a bias of −1 V. The inset shows the current measurement conditions.

local presence of large electric fields and the FIRC effect at the Au needle tips.

To validate the predicted enhancement of CO_2RR by FIRC, we explored the CO_2 reduction activity of Au needles, rods and particles in CO_2-saturated 0.5 M $KHCO_3$ (pH 7.2). Products were quantified using gas chromatography. The linear sweep voltammetry curves exhibit a clear reduction peak for the Au needles in the range −0.30 V to −0.50 V (Fig. 4a), whereas Au rods and particles only give smooth current–voltage curves. Notably, Au needles exhibited a stable total geometric current density (j_{tot}) of approximately 15 mA cm^{-2} at a potential of −0.35 V (corresponding to an overpotential η_{CO} of 0.24 V for CO production[4,9]) during 8 h of continuous reaction (Fig. 4b). The Faradaic efficiency for CO production was nearly quantitative (>95%) throughout the electrocatalytic process. No obvious changes in the morphology, crystal structure and surface state were observed after long-term CO_2RR (Extended Data Fig. 5a), indicating that the Au needles are stable under electrocatalytic conditions. Au rods and particles exhibited j_{tot} values of approximately 0.7 mA cm^{-2} and 0.1 mA cm^{-2} after 8 h of reaction. Their Faradaic efficiencies for CO were about 25% and 3%, respectively. The approximately 20-fold difference in CO_2RR current between Au needles and Au rods agrees with the increase in surface-adsorbed K^+ ion concentration and current density predicted by theory (Fig. 2d).

The differences in CO_2 reduction activity among Au needles, rods and particles were more pronounced at lower overpotentials. At −0.3 V ($\eta_{CO}=0.19$ V), Au needles exhibited $j_{tot} \approx 7$ mA cm^{-2} over the course of 8 h of electrolysis and about 90% Faradaic efficiency for CO production (Extended Data Fig. 3h), while Au particles exhibited very low current densities (<0.05 mA cm^{-2}) and exclusively H_2 evolution. Au rods also showed a low current density of about 0.1 mA cm^{-2} and a very poor ~3% selectivity for CO formation (Extended Data Fig. 3h). No detectable CO_2 reduction was observed for Au rods at applied potentials closer to RHE than −0.3 V, whereas Au needles continued to reduce CO_2—at −0.2 V ($\eta_{CO}=0.09$ V), Au needles gave a j_{tot} value of about 0.6 mA cm^{-2} with a Faradaic efficiency of about 40% for CO (Extended Data Fig. 3i), and at the exceptionally low potential of −0.18 V ($\eta_{CO}=0.07$ V) the CO product remained readily detectable using gas chromatography (Faradaic efficiency of about 6%). A summary of CO_2 reduction Faradaic efficiencies at potentials between −0.18 V and −0.5 V for the different systems is given in Fig. 4c.

Intrinsic performances can be compared by considering the geometric and the electrochemical active surface area (ECSA)-normalized partial current densities for CO production (geometric current density j_{CO}) versus applied potential for the three classes of electrodes (Extended Data Fig. 3j, k). Once current is renormalized by the ECSA, the j_{CO} value measured at −0.35 V on Au needles is 63 times higher than on rods and 112 times higher than on particles (Extended Data Fig. 3j, k), indicating higher intrinsic CO_2RR activities for Au needles.

Tafel analysis (Fig. 4d) gives for Au needles, rods and particles a slope of 42 mV dec^{-1}, 80 mV dec^{-1} and 96 mV dec^{-1}, respectively. Previous studies suggest that during two-electron CO_2RR, the first one-electron step of CO_2 to COOH* or $CO_2^{\bullet -}$ intermediates is determining the rate for the combined process[6–8] and hence the Tafel slope. The Tafel slope measured for the gold particles of 96 mV dec^{-1} agrees well with prior reports[9,15] (114 mV dec^{-1} and 129 mV dec^{-1}), whereas the much lower Tafel slope of 42 mV dec^{-1} obtained for the needles indicates a faster first-electron transfer step[9,16,17] and confirms the superiority of Au needles in CO_2 reduction. These observations agree with the FIRC picture of Au needles concentrating CO_2 at the electrode and with modelled Tafel slopes that assume cathodic charge transfer coefficients are 0.95,

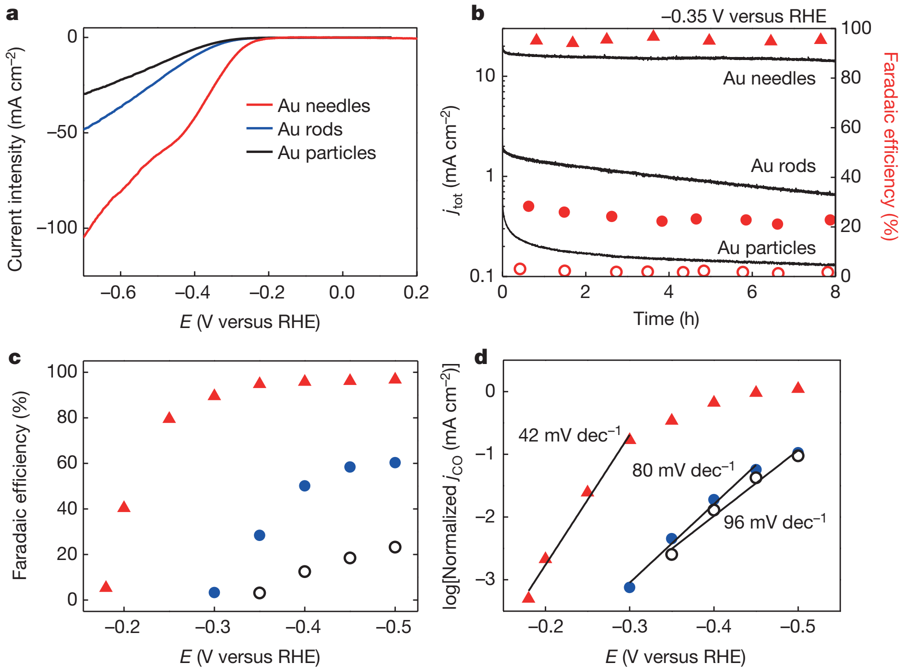

Figure 4 | CO_2 reduction performances on Au needles, rods and particles in 0.5 M $KHCO_3$, pH 7.2. a, Current–voltage curves on Au needles, rods and particles obtained from the linear sweep volatmmetry scans. Scan rate, 10 mV s^{-1}. **b,** CO_2 reduction activity of Au needles, rods and particles at −0.35 V versus RHE. Total current density (left axis) versus time and CO Faradaic efficiency (right axis) versus time. **c,** CO Faradaic efficiencies on Au needles, rods and particles at different applied potentials. **d,** ECSA-normalized CO production partial current density versus potential on Au needles, rods and particles.

0.49 and 0.43 for Au needles, rods and particles, respectively (Extended Data Fig. 2f).

To assess the energy barriers, we studied the effect of temperature on the performance of the catalysts (Extended Data Fig. 3l–n) and found the rate constants to follow the Arrhenius relationship. The electrochemical activation energies of 72 kJ mol^{-1}, 44 kJ mol^{-1} and 21 kJ mol^{-1} extracted for particles, rods and needles from the slope of their Arrhenius plots at $\eta = 240$ mV (see the insets of Extended Data Fig. 3l–n) are comparable to those reported previously (Extended Data Table 2)[18–22], with the lowest value for Au needles highlighting the dominant role of thermodynamics in the CO_2RR.

To probe charge transfer processes occurring at electrode/solution interfaces, we obtained electrochemical impedance (Z) spectra (Extended Data Fig. 3g and Extended Data Table 2). For Au needles, the semicircle diameter of the Nyquist plot is much smaller, reflecting an acceleration of the charge transfer process. Thus, both charge separation and the kinetics of charge transfer on Au needles are improved.

Specific facets, grain boundaries, metastable surfaces, corner and edge sites have all previously been invoked as structural features that enhance CO_2-to-CO electroreduction activity[8,9,23–26]. To test whether these could account for the higher intrinsic activity of the Au needles, in one experiment we overcoated the needles with additional Au thin layers; in a second we annealed the Au needles in vacuum; in a third, we used etching solutions designed to expose (111) facets preferentially[27]; and in a fourth, we used plasma bombardment to produce fresh reconstructions (Extended Data Fig. 5b–e). None of these surface-manipulating treatments affected the activity of Au needles (all performance remained within 10% of the original), so we conclude that the primary benefits of the needles in CO_2RR are not related to the details of surface faceting nor of atomic-scale structure.

We systematically varied the nanostructure morphologies. When we grew dendritic Au nanoleaves, we obtained a low j_{CO} value and Faradaic efficiency, which we attribute to their high radius (50–500 nm) of curvature (Extended Data Fig. 6). When we dulled the needles by electrodepositing a thick additional Au layer, the large-radius (50–100 nm) nanoparticles covering the tips led to notably worsened performance in CO_2RR even though the ECSA had been increased 1.7-fold owing to the attached nanoparticles (Extended Data Fig. 5g and h). Electrochemical oxidation of Au needles further dulls the tips of the needles and the CO_2RR performance was further decreased even though oxide-derived Au was generated on the surface (Extended Data Fig. 4e–j)[9].

Further experiments performed at different K^+ concentrations confirm that CO_2RR performance increases with K^+ concentration (Extended Data Fig. 7a, b). Notably, Au needles exhibited a j_{co} of approximately 22 mA cm^{-2} at −0.35 V after 8 h by using a saturated $KHCO_3$ solution (Extended Data Fig. 7c). The long-term steady-state CO_2 reduction current density for the highest-performing Au needle morphology is over one order of magnitude higher at −0.35 V than for any previously reported CO_2 reduction catalysts in aqueous solution with inorganic electrolyte (Extended Data Table 3); this comparison takes into account the best nanostructured oxide-derived gold electrodes[9,23–25].

We also carried out CO_2RR experiments in solutions without alkali cations, such as CO_2 saturated NH_4HCO_3 solution and H_2O (Extended Data Fig. 7e, f). The results show that the current density and selectivity decreased substantially, and only H_2 was generated in pure H_2O and was accompanied by a very small current density. The results, taken together, confirm that the FIRC dictates the CO_2RR rate.

To demonstrate the universality of the FIRC, we prepared palladium (Pd) needles and tested their CO_2RR performance (Extended Data Fig. 8). The obtained Pd needles exhibited enhanced CO_2-to-formate conversion compared with that of rods and particles. Pd needles exhibited a stable geometric current density $j_{formate}$ of approximately 10 mA cm^{-2} at −0.2 V over the course of 20 h in 0.5 M $KHCO_3$ solution (Extended Data Fig. 8). Faradaic efficiency for formate generation was nearly quantitative (>91%) throughout the electrocatalytic process. This formate production current density on Pd needles is over three times higher at −0.2 V than the previously reported CO_2-to-formate catalysts in aqueous solution (Extended Data Table 3)[2,28], confirming that the FIRC concept can be extended to other CO_2RR systems.

The sharp-tip enhancement effect may have contributed to previous studies identifying particularly active CO_2RR sites at corners[8] and ridges[24,25], since such sites are locally high-curvature regions. It remains to be explored whether it will be effective in industrial electrolysers operating at current densities of 300 mA cm^{-2} (that is, with reaction rates ten times faster than studied here), but enhanced control over the density of sharp tips and use of high bulk CO_2 concentrations could enhance CO_2RR rates further towards the goal of industrial electrosynthesis of carbon-based fuels. In a wider electrochemistry context, the tip-enhanced field phenomenon can be extended to concentrate the reagents locally in other reactions and as such suggests a general principle for the design of efficient electrodes for catalysis.

Online Content Methods, along with any additional Extended Data display items and Source Data, are available in the online version of the paper; references unique to these sections appear only in the online paper.

Received 30 November 2015; accepted 15 June 2016.
Published online 3 August 2016.

1. Costentin, C., Drouet, S., Robert, M. & Saveant, J. M. A local proton source enhances CO_2 electroreduction to CO by a molecular Fe catalyst. *Science* **338,** 90–94 (2012).
2. Gao, S. *et al.* Partially oxidized atomic cobalt layers for carbon dioxide electroreduction to liquid fuel. *Nature* **529,** 68–71 (2016).
3. Lin, S. *et al.* Covalent organic frameworks comprising cobalt porphyrins for catalytic CO_2 reduction in water. *Science* **349,** 1208–1213 (2015).
4. Rosen, B. A. *et al.* Ionic liquid-mediated selective conversion of CO_2 to CO at low overpotentials. *Science* **334,** 643–644 (2011).
5. Qiao, J. L., Liu, Y. Y., Hong, F. & Zhang, J. J. A review of catalysts for the electroreduction of carbon dioxide to produce low-carbon fuels. *Chem. Soc. Rev.* **43,** 631–675 (2014).
6. Hori, Y. in *Modern Aspects of Electrochemistry* Vol. 42 (eds Vayenas, C. *et al.*) 89–189 (Springer, 2008).
7. Lu, Q. *et al.* A selective and efficient electrocatalyst for carbon dioxide reduction. *Nat. Commun.* **5,** 3242 (2014).
8. Back, S., Yeom, M. S. & Jung, Y. Active sites of Au and Ag nanoparticle catalysts for CO_2 electroreduction to CO. *ACS Catal.* **5,** 5089–5096 (2015).
9. Chen, Y., Li, C. W. & Kanan, M. W. Aqueous CO_2 reduction at very low overpotential on oxide-derived Au nanoparticles. *J. Am. Chem. Soc.* **134,** 19969–19972 (2012).
10. Varela, A. S., Kroschel, M., Reier, T. & Strasser, P. Controlling the selectivity of CO_2 electroreduction on copper: the effect of the electrolyte concentration and the importance of the local pH. *Catal. Today* **260,** 8–13 (2016).
11. Kokoszka, B., Jarrah, N. K., Liu, C., Moore, D. T. & Landskron, K. Supercapacitive swing adsorption of carbon dioxide. *Angew. Chem. Int. Ed.* **53,** 3698–3701 (2014).
12. Jackson, J. D. *Classical Electrodynamics* Vol. 3, 75–79 (Wiley, 1962).
13. Soleymani, L., Fang, Z., Sargent, E. H. & Kelley, S. O. Programming the detection limits of biosensors through controlled nanostructuring. *Nat. Nanotechnol.* **4,** 844–848 (2009).
14. Das, J. & Kelley, S. O. Tuning the bacterial detection sensitivity of nanostructured microelectrodes. *Anal. Chem.* **85,** 7333–7338 (2013).
15. Noda, H., Ikeda, S., Yamamoto, A., Einaga, H. & Ito, K. Kinetics of electrochemcial reduction of carbon-dioxide on a gold electrode in phosphate buffer solutions. *Bull. Chem. Soc. Jpn.* **68,** 1889–1895 (1995).
16. Gileadi, E. *Electrode Kinetics for Chemists, Engineers, and Materials Scientists* Ch. 1 (VCH, 1993).
17. Chen, Y. H. & Kanan, M. W. Tin oxide dependence of the CO_2 reduction efficiency on tin electrodes and enhanced activity for tin/tin oxide thin-film catalysts. *J. Am. Chem. Soc.* **134,** 1986–1989 (2012).
18. Morris, A. J., McGibbon, R. T. & Bocarsly, A. B. Electrocatalytic carbon dioxide activation: the rate-determining step of pyridinium-catalyzed CO_2 reduction. *ChemSusChem* **4,** 191–196 (2011).
19. Peebles, D. E., Goodman, D. W. & White, J. M. Methanation of carbon dioxide on nickel(100) and the effects of surface modifiers. *J. Phys. Chem.* **87,** 4378–4387 (1983).
20. Wang, W., Wang, S., Ma, X. & Gong, J. Recent advances in catalytic hydrogenation of carbon dioxide. *Chem. Soc. Rev.* **40,** 3703–3727 (2011).
21. Ghuman, K. K. *et al.* Illuminating CO_2 reduction on frustrated Lewis pair surfaces: investigating the role of surface hydroxides and oxygen vacancies on nanocrystalline $In_2O_{3-x}(OH)_y$. *Phys. Chem. Chem. Phys.* **17,** 14623–14635 (2015).
22. Schmeier, T. J., Dobereiner, G. E., Crabtree, R. H. & Hazari, N. Secondary coordination sphere interactions facilitate the insertion step in an iridium(III) CO_2 reduction catalyst. *J. Am. Chem. Soc.* **133,** 9274–9277 (2011).
23. Feng, X. F., Jiang, K. L., Fan, S. S. & Kanan, M. W. Grain-boundary-dependent CO_2 electroreduction activity. *J. Am. Chem. Soc.* **137,** 4606–4609 (2015).
24. Zhu, W. *et al.* Monodisperse Au nanoparticles for selective electrocatalytic reduction of CO_2 to CO. *J. Am. Chem. Soc.* **135,** 16833–16836 (2013).
25. Zhu, W. L. *et al.* Active and selective conversion of CO_2 to CO on ultrathin Au nanowires. *J. Am. Chem. Soc.* **136,** 16132–16135 (2014).
26. Zhang, Q. & Wang, H. Facet-dependent catalytic activities of Au nanoparticles enclosed by high-index facets. *ACS Catal.* **4,** 4027–4033 (2014).
27. Mettela, G. & Kulkarni, G. U. Facet selective etching of Au microcrystallites. *Nano Res.* **8,** 2925–2934 (2015).
28. Min, X. & Kanan, M. W. Pd-catalyzed electrohydrogenation of carbon dioxide to formate: high mass activity at low overpotential and identification of the deactivation pathway. *J. Am. Chem. Soc.* **137,** 4701–4708 (2015).

Acknowledgements This work was supported by the Ontario Research Fund: Research Excellence programme, the Natural Sciences and Engineering Research Council (NSERC) of Canada, the CIFAR Bio-Inspired Solar Energy programme and a University of Toronto Connaught grant. B.Z. acknowledges funding from Shanghai Municipal Natural Science Foundation (14ZR1410200) and the National Natural Science Foundation of China (21503079). We thank X. Lan, P. Kanjanaboos, G. Walters, L. Levina, R. Wolowiec, D. Kopilovic, E. Palmiano, T. Burdyny and J. Tam from the University of Toronto for Au electron beam deposition, liquid products testing, AFM testing, TEM EELS measurements, discussions and additional aids during the course of study, Y. Tian from the King Abdullah University of Science and Technology for electrode preparation assistance, and M. Bajdich, L. D. Chen and K. Chan from Stanford University for advice on DFT calculations. This work has also benefited from the Spherical Grating Monochromator beamlines at the Canadian Light Source. DFT calculations were performed on the IBM BlueGene Q supercomputer with support from the Southern Ontario Smart Computing Innovation Platform (SOSCIP).

Author Contributions E.H.S., S.O.K. and D.S. supervised the project. M.L., Y.P. and B.Z. designed and carried out all the experiments and COMSOL simulations. P.D.L. and O.V. carried out the DFT simulation. All authors discussed the results and assisted during manuscript preparation.

Author Information Reprints and permissions information is available at www.nature.com/reprints. The authors declare no competing financial interests. Readers are welcome to comment on the online version of the paper. Correspondence and requests for materials should be addressed to E.H.S. (ted.sargent@utoronto.ca).

METHODS

DFT calculations. DFT calculations were performed on 3 × 3 × 3 slabs of Au(111), Au(110), Au(100), and Au(211) using the generalized gradient approximation exchange correlation functional of ref. 29. All DFT simulations were performed with the Vienna *ab initio* Simulation Package (VASP)[30] using the projector augmented wave method[31]. The projector augmented wave pseudopotentials[31,32] were used to calculate the interaction between ions and electrons in a plane wave basis set with a cut-off energy of 500 eV and a 5 × 5 × 1 Monkhorst–Pack mesh[33] used for *k*-point sampling and a Fermi-level smearing of 0.1 eV. Spin polarization was included as it has been previously shown to be important for binding energies on gold nanoparticles and surfaces[34]. The surface slabs were modelled with 10 Å of vacuum and dipole corrections were implemented. Structural optimizations were performed with the Broyden–Fletcher–Goldfarb–Shanno[45] (BFGS) algorithm until the maximum force was less than 0.02 eV per atom, with the surface slab fully relaxed. Once the slab models were optimized, all subsequent thermodynamic calculations were performed with the bottom two layers fixed.

All thermodynamic properties were calculated using the open-source atomic simulation environment suite of programs[35]. The Gibbs free energies were calculated at 298 K and 1 atm as outlined below:

$$G = H - T\Delta S = E_{\mathrm{DFT}} + E_{\mathrm{ZPE}} + \int_0^{298} C_{\mathrm{v}}\mathrm{d}T - T\Delta S$$

where E_{DFT} is the DFT-optimized total energy, E_{ZPE} is the zero-point vibrational energy, $\int_0^{298} C_{\mathrm{v}}\mathrm{d}T$ is the heat capacity, T is the temperature, and ΔS is the entropy. Gas-phase molecules such as CO_2 and H_2 were treated using the ideal gas approximation, whereas adsorbates were treated using a harmonic approximation. The DFT-calculated energy for CO_2 was corrected by 0.45 eV, a common adjustment to account for an overestimation by DFT[36]. The change in Gibbs free energy ΔG between reaction steps of the CO_2 to CO reaction coordinate was calculated from the computational hydrogen electrode model[37]. Additionally, the binding energy was calculated from DFT-optimized structures as follows: $E_{\mathrm{binding}} = E_{\mathrm{CO2*}} - (E_{\mathrm{Au}} + E_{\mathrm{CO2}})$ where $E_{\mathrm{CO2*}}$ is the energy of the system with CO_2 proximate to the Au surface, E_{Au} is the energy of the gold surface (with and without K^+ for the respective cases), and E_{CO2} is the gas-phase energy of CO_2.

Charge density analysis was performed from the electron density as calculated from DFT. The volume slice was visualized in Visual Molecular Dynamics (VMD, http://www.ks.uiuc.edu/Research/vmd/) with an isovalue of 0.5 (ref. 38). Bader partial atomic charges were calculated using the Bader Charge Analysis code as maintained by the Henkelman group[39].

***Ab initio* molecular dynamics simulations.** All *ab initio* molecular dynamics simulations on 6 × 6 × 5 slabs of Au(111), Au(110), Au(100) and Au(211) were performed within the DFT framework as mentioned above with a cut-off energy of 400 eV and gamma *k*-point sampling of the Brillouin zone. The electronic self-consistent loop was considered to be converged if the energy difference was lower than 10^{-5} eV, at which point the molecular dynamics would continue to the next time step. A canonical ensemble using a Nosé–Hoover thermostat was used with a constant temperature of 300 K. Fermi-smearing was used owing to the presence of the Au(111) metal surface, with 0.2 eV used as the width of smearing. A 5-ps total simulation run was performed with 1-ps equilibration and 4-ps production runs and a time step of 1 fs for 5,000 steps. An ensemble average of the radial distribution function and mean square displacement was obtained from 25 unique runs starting from the same initial configuration in order to better sample the binding event of CO_2 to Au.

COMSOL Multiphysics simulations. Free electron density on the electrodes, as well as the electric field and potassium ion density within the vicinity of the electrodes was simulated using the COMSOL Multiphysics finite-element-based solver (https://www.comsol.com/). The 'Electric currents' module was used to solve the free electron density on the electrode under a specific electrode bias potential. Electric field $\boldsymbol{E}$ was computed as the opposite gradient of the electric potential V as follows: $\boldsymbol{E} = -\boldsymbol{\nabla} V$.

The electric conductivity of the electrode (gold) was taken to be 4.42×10^7 S m^{-1} (ref. 40). The electrolyte conductivity was assumed to be 10 S m^{-1}. Charge density ρ was computed using Gauss's law for electric field: $\rho = \varepsilon_{\mathrm{r}}\varepsilon_0 \boldsymbol{\nabla} \cdot \boldsymbol{E}$, where ε_0 represents the dielectric function for a vacuum, and ε_{r} represents the dielectric function of the materials, and equals 78 for the electrolyte and 1 for gold.

In this work, the electrical double layer was modelled using the Gouy–Chapman–Stern model, which consists of a Helmholtz layer and a diffusion layer (illustrated in Extended Data Fig. 2a). The Helmholtz layer consists of a monolayer of surface-adsorbed hydrated cation on the electrode surface, which speeds up the CO_2RR. The diffusion layer consists of both cations and anions, which freely diffuse in the electrolyte and form concentration gradients towards and away from the electrode surface. The diffusion layer was established as the result of a dynamic equilibrium between electrostatic forces and diffusion (that is, the 'entropic forces'). The 'Electrostatics' and the 'Transport of diluted species' modules were combined to solve the potassium ion density in the electrical double layer. The Poisson–Nerst–Planck equations were solved in the steady state:

$$\nabla^2 V = \begin{cases} 0 & d < d_{\mathrm{H}} \\ (c_{\mathrm{K}} - c_{\mathrm{HCO_3}})F & d > d_{\mathrm{H}} \end{cases}$$

$$\boldsymbol{\nabla} \cdot \left(D\boldsymbol{\nabla} c_i + \frac{D z_i e}{k_{\mathrm{B}}T} c_i \boldsymbol{\nabla} V \right) = 0$$

Here d is the distance from the electrode surface into the electrolyte, and d_{H} is the thickness of the Helmholtz layer, which is taken as the radius of a hydrated potassium ion (0.33 nm)[41]. That is, $d < d_{\mathrm{H}}$ within the Helmholtz layer, and $d > d_{\mathrm{H}}$ in the diffusion layer. c_i with $i \in \{K^+, HCO_3^-\}$ are the concentrations of the potassium or bicarbonate ion, z_i are the valencies of both ions, e is the elementary charge, k_{B} is Boltzmann constant, the absolute temperature T was taken is 297.3 K. The diffusion coefficients D of the potassium ion, the bicarbonate ion, and the proton in water were taken to be 2.14×10^{-9} m^2 s^{-1}, 7.02×10^{-9} m^2 s^{-1} and 7.10×10^{-9} m^2 s^{-1} (ref. 42). Two-dimensional axisymmetric models were built to represent the three-dimensional nanoneedle, nanorod and nanoparticle structures used in this work. Triangular meshes were used for all simulations. Meshes were set to be the densest at the surface of the electrodes, where the element size was 0.17 nm. In other parts of the model where less precision is required, for example, in the bulk electrolyte, the maximum element size was 20 nm.

The electrochemical module in COMSOL was used to obtain the CO_2 to CO reaction current density using the Butler–Volmer equation:

$$i = i_0\left[\exp\left(\frac{\alpha_{\mathrm{a}} nF\eta}{RT}\right) - \exp\left(-\frac{\alpha_{\mathrm{c}} nF\eta}{RT}\right)\right]$$

where α_{a} and α_{c} are the dimensionless anodic and cathodic charge transfer coefficients, respectively, $n = 2$ is the number of electrons involved in the electrode reaction, F is the Faraday constant, R is the universal gas constant, and T is temperature, taken to be 293.15 K. The exchange current density i_0 obeys the Arrhenius law:

$$i_0 \propto \exp\left(-\frac{E_{\mathrm{a}}}{k_{\mathrm{B}}T}\right)$$

where k_{B} is the Boltzmann constant, and E_{a} is the activation energy of the CO_2 to CO reaction, which was experimentally obtained to be 0.59 eV without K^+, and 0.21 eV with K^+.

Preparation of gold needle, rod, particle and leaf electrodes. Gold electrodes were prepared through an electrodeposition process using a solution containing $HAuCl_4$ (99.99% Sigma) and HCl (TraceSELECT) solution[13]. The concentration of HCl was fixed at 0.5 mol l^{-1} (M). Gold-coated slides (for characterization, EMF Corporation) and carbon paper (for CO_2RR performance measurement, Toray TGP-H-060, purchased from Fuel Cell Store) were used as substrates (0.1–0.3 cm^2). The Au needle electrode was formed using a 160 mM $HAuCl_4$ solution and direct current potential amperometry at −400 mV for 300 s. Au particle, rod and leaf electrodes were formed using direct current potential amperometry at −250 mV with 13 mM, 26 mM and 40 mM $HAuCl_4$ solutions for 1,200 s, 900 s and 600 s, respectively.

Preparation of palladium needle, rod and particle electrodes. Pd needles were synthesized by a two-step potential square wave electrodeposition in a solution of 2 mM K_2PdCl_6 in 0.5 M H_2SO_4 (ref. 43) on an Autolab PGSTAT302N potentiostat. In the first step, E_1, T_1, E_2 and T_2 were 0.8 V, 0.05 s, −0.7 V and 0.02 s, respectively. The number of square waves was 1,200. For the second step E_1, T_1, E_2 and T_2 were 0.6 V, 0.005 s, 0.25 V and 0.005 s, respectively. The number of square waves was 100,000. For the preparation of Pd rods, E_1 was set at 0.2 V with the number of square waves being 50,000 in the second step. All other parameters remained the same as for the Pd needles. For preparation of Pd particles, only the first step for Pd needle deposition was applied and the square wave number was set to 50,000.

Au secondary electrodeposition. After washing with deionized water and drying, Au needles, rods and particles were coated with a thin layer of Au by electrodeposition in a solution of 20 mM $HAuCl_4$ and 0.5 M $HClO_4$. The secondary deposition was performed by using direct current potential amperometry at −400 mV for 30 s.

Surface, grain boundaries and Au oxide investigation. To exclude the influence of the surface states, such as surface facets, corner sites and edge sites, a uniform Au thin layer with thickness of 10 nm was deposited on Au needles, rods and particles by using electron-beam deposition with a rate of 0.4 Å s^{-1}. The surface of Au needles were also etched by using $CuCl_2$ solution (5 mM)[27]. Briefly, Au nanoneedles was immersed in a vial containing 15 ml of $CuCl_2$ solution (5 mM). The vial was then heated to 70 °C using an oil bath and kept at that temperature for 1 h. The etched Au nanoneedles obtained were washed with a copious amount of water and dried at room temperature.

To investigate the influence of grain boundaries and metastable surface states, the Au needle electrode was annealed at 140 °C in vacuum for 24 h and treated with plasma bombardment for 1 h (50 W, argon atmosphere). To investigate the influence of Au oxide, Au needles were oxidized in aqueous 0.5 M H_2SO_4 at 1.5 V versus Ag/AgCl for 10 h.

ECSA measurement. We used two methods to estimate the ECSA of Au needles, rods and particles. In the first we integrated the reduction peak area obtained from a cyclic voltammogram in 50 mM H_2SO_4 (ref. 44). In the second, we measured the charge associated with the stripping of an underpotential-deposited Cu monolayer[9]. In the first method, cyclic voltammograms from 0 V to 1.5 V (versus Ag/AgCl) at a scan rate of 50 mV s^{-1} were acquired repeatedly until the traces converged. In the forward scan, a monolayer of chemisorbed oxygen is formed and then it is reduced in the reverse scan. The surface area was calculated by integrating the reduction peak (0.9 V versus Ag/AgCl) to obtain the reduction charge. The reduction charge per microscopic unit area has been experimentally determined to be 448 μC cm^{-2}.

In the underpotential-deposited method, the electrode was immersed in a 0.50 M H_2SO_4 solution containing 100 mM $CuSO_4$ continuously purged with N_2. Cyclic voltammograms from 0.83 V to 0.483 V (versus Ag/AgCl) at a scan rate of 50 mV s^{-1} were acquired repeatedly until traces converged. The anodic stripping waves at 0.403 V versus Ag/AgCl were integrated. The factor used to convert the stripping charge to surface area was 92.4 μC cm^{-2}. The error of the results obtained from these two methods are within 5%, indicating an accurate estimation of ECSA.

Electric-field-induced adsorbed K^+. Electric-field-induced adsorbed K^+ was performed in 0.5 M $KHCO_3$ solution. Au needles, rods and particles were run in the solution at −1 V. Once the running time reached 120 s, the electrode was directly raised above the solution. After removing the applied potential, the electrodes were immersed in 10 ml pure water and any adsorbed K^+ on the Au needles was released into the pure water. Then, the amount of K^+ in the water was checked using an inductively coupled plasma optical emission spectrometer (ICP-OES, Agilent Dual-View 720 with a charge-coupled device (CCD) detector for full wavelength coverage between 167 nm and 785 nm). The obtained results were normalized by using ECSA.

Characterization. The structural characteristics of the prepared samples were measured by powder X-ray diffraction at room temperature on a MiniFlex600 instrument with a copper target ($\lambda = 1.54056$ Å). The morphologies of the prepared Au electrodes were investigated using SEM on a Hitachi SU-8230 apparatus and TEM on a Hitachi HF-3300 instrument with an acceleration voltage of 200 kV. Compositions were studied by X-ray photoelectron spectroscopy (model 5600, Perkin-Elmer). The binding energy data were calibrated with reference to the C 1*s* signal at 284.5 eV. Kelvin probe atomic force microscopy images were obtained using an Asylum Research MFP-3D instrument. Electrostatic field $\boldsymbol{E}$ around the electrodes was calculated to have the opposite gradient of the electric potential raw data V from Kelvin probe atomic force microscopy imaging: $\boldsymbol{E} = -\boldsymbol{\nabla} V$. Currents on single Au needle, rod and particle were measured by using a Cypher ES instrument with a conductive model. Before current measurement, a 10-nm-thick layer of TiO_2 was deposited on the surface of Au needles, rods and particles using a Picosun R200 atomic layer deposition system. Soft X-ray absorption measurements were performed at the Spherical Grating Monochromator beamline of the Canadian Light Source in Saskatoon.

Electrocatalytic reduction of CO_2. All CO_2 reduction experiments were performed using a three-electrode system connected to an electrochemical workstation (Autolab PGSTAT302N). Ag/AgCl (with saturated KCl as the filling solution) and platinum mesh were used as reference and counter electrodes, respectively. Electrode potentials were converted to the reversible hydrogen electrode (RHE) reference scale using $E_{RHE} = E_{Ag/AgCl} + 0.197\,V + 0.0591 \times pH$.

The electrolyte was 0.5 M $KHCO_3$ saturated with CO_2 with pH of 7.2. The experiments were performed in a gas-tight two-compartment H-cell separated by an ion exchange membrane (Nafion117). The electrolyte in the cathodic compartment was stirred at a rate of 300 r.p.m. during electrolysis. CO_2 gas was delivered into the cathodic compartment at a rate of 5.00 standard cubic centimeters per minute (s.c.c.m.) and was routed into a gas chromatograph (PerkinElmer Clarus 600). The gas chromatograph was equipped with a Molecular Sieve 5A capillary column and a packed Carboxen-1000 column. Argon (Linde, 99.999%) was used as the carrier gas. The gas chromatograph columns led directly to a thermal conductivity detector to quantify hydrogen and a flame ionization detector equipped with a methanizer to quantify carbon monoxide. The partial current densities of CO and H_2 production were calculated from the gas chromatograph peak areas as below[9]:

$$j_{co} = \frac{\text{peak area}}{\alpha} \times \text{flow rate} \times \frac{2Fp_0}{RT} \times (\text{electrode area})^{-1}$$

$$j_{H_2} = \frac{\text{peak area}}{\beta} \times \text{flow rate} \times \frac{2Fp_0}{RT} \times (\text{electrode area})^{-1}$$

where α and β are conversion factors for CO and H_2 respectively based on calibration of the gas chromatograph with standard samples, $p_0 = 1.013$ bar and $T = 300$ K.

Formate was quantified on a gas chromatograph with mass spectrometry (PerkinElmer Clarus 600 GC-MS System). Assuming that two electrons are needed to produce one formate molecule, the Faradaic efficiency was calculated as $2Fn_{formate}/Q = 2Fn_{formate}/(It)$, where F is the Faraday constant, I is the current, t is the running time and $n_{formate}$ is the total amount of produced formate (in moles).

29. Perdew, J. P., Burke, K. & Ernzerhof, M. Generalized gradient approximation made simple. *Phys. Rev. Lett.* **77,** 3865–3868 (1996).
30. Kresse, G. & Furthmuller, J. Efficient iterative schemes for *ab initio* total-energy calculations using a plane-wave basis set. *Phys. Rev. B* **54,** 11169–11186 (1996).
31. Blöchl, P. E. Projector augmented-wave method. *Phys. Rev. B* **50,** 17953–17979 (1994).
32. Kresse, G. & Joubert, D. From ultrasoft pseudopotentials to the projector augmented-wave method. *Phys. Rev. B* **59,** 1758–1775 (1999).
33. Monkhorst, H. J. & Pack, J. D. Special points for Brillouin-zone integrations. *Phys. Rev. B* **13,** 5188–5192 (1976).
34. Kleis, J. *et al.* Finite size effects in chemical bonding: from small clusters to solids. *Catal. Lett.* **141,** 1067–1071 (2011).
35. Bahn, S. R. & Jacobsen, K. W. An object-oriented scripting interface to a legacy electronic structure code. *Comput. Sci. Eng.* **4,** 56–66 (2002).
36. Studt, F. *et al.* The mechanism of CO and CO_2 hydrogenation to methanol over Cu-based catalysts. *ChemCatChem* **7,** 1105–1111 (2015).
37. Peterson, A. A., Abild-Pedersen, F., Studt, F., Rossmeisl, J. & Norskov, J. K. How copper catalyzes the electroreduction of carbon dioxide into hydrocarbon fuels. *Energy Environ. Sci.* **3,** 1311–1315 (2010).
38. Humphrey, W., Dalke, A. & Schulten, K. VMD: visual molecular dynamics. *J. Mol. Graph.* **14,** 33–38 (1996).
39. Tang, W., Sanville, E. & Henkelman, G. A grid-based Bader analysis algorithm without lattice bias. *J. Phys. Condens. Matter* **21,** 084204 (2009).
40. Serway, R. A. & Jewett, J. W. *Principles of Physics* Vol. 1, 602 (Saunders College Pub., 1998).
41. Wang, H. & Pilon, L. Accurate simulations of electric double layer capacitance of ultramicroelectrodes. *J. Phys. Chem. C* **115,** 16711–16719 (2011).
42. Friedman, A. M. & Kennedy, J. W. The self-diffusion coefficients of potassium, cesium, iodide and chloride ions in aqueous solutions. *J. Am. Chem. Soc.* **77,** 4499–4501 (1955).
43. Meng, H., Wang, C., Shen, P. K. & Wu, G. Palladium thorn clusters as catalysts for electrooxidation of formic acid. *Energy Environ. Sci.* **4,** 1522–1526 (2011).
44. Bin, X. M., Sargent, E. H. & Kelley, S. O. Nanostructuring of sensors determines the efficiency of biomolecular capture. *Anal. Chem.* **82,** 5928–5931 (2010).
45. Head, J. D. & Zerner, M. C. A Broyden–Fletcher–Goldfarb–Shanno optimization procedure for molecular geometries. *Chem. Phys. Lett.* **122,** 264–270 (1985).

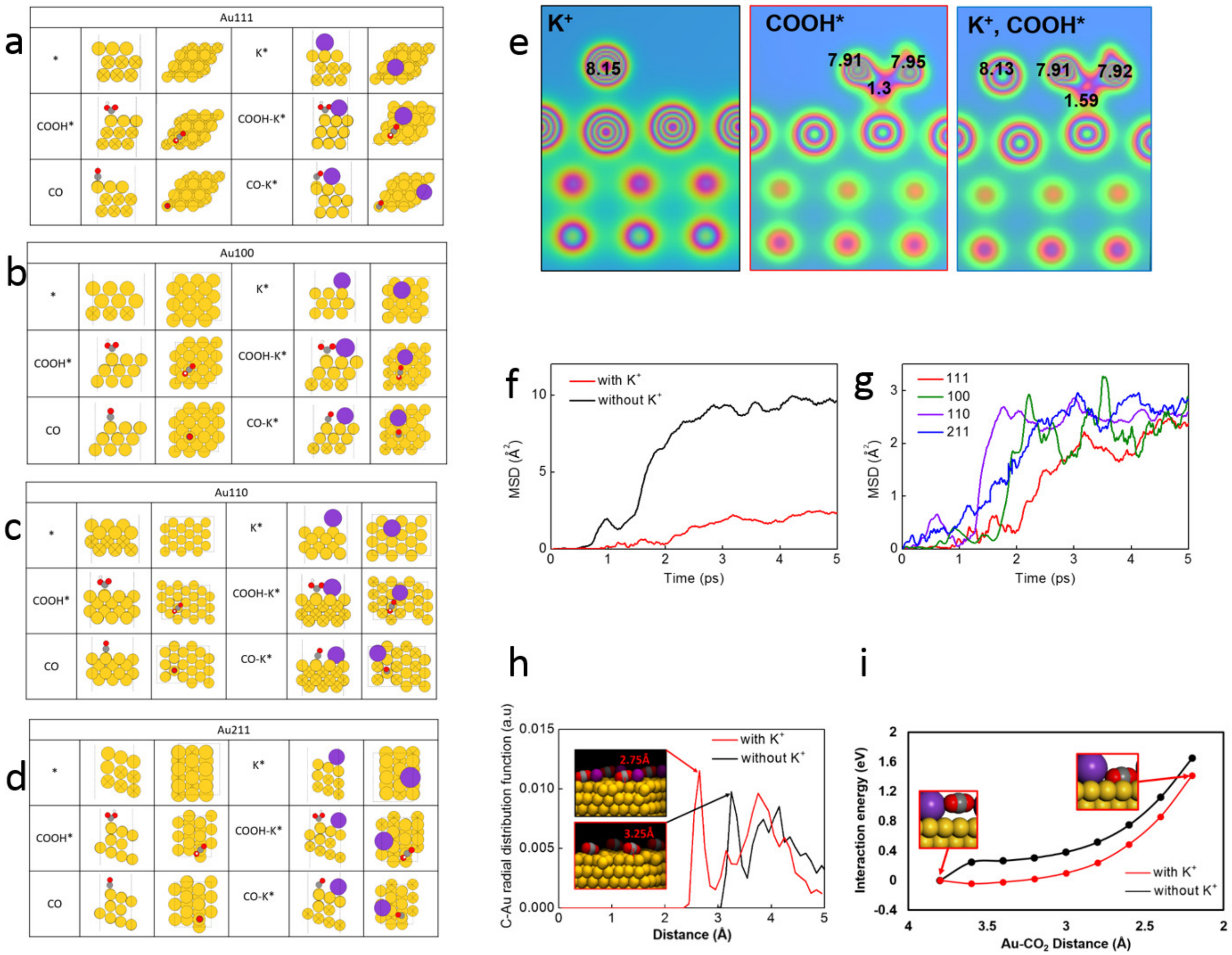

Extended Data Figure 1 | Optimized structure for Au facets and data calculated with or without K^+. **a**–**d**, Optimized structures. **a**, Au(111) facet. **b**, Au(100) facet. **c**, Au(110) facet. **d**, Au(211) facet. Included are the optimized positions of the adsorbates COOH and CO without and with the presence of an adsorbed K^+ (purple). **e**, Volume slice of calculated charge densities. Bader partial atomic charges are indicated in black with and without K^+. In the presence of K^+ the Bader partial atomic charge on the carbon of COOH* has increased from 1.3 to 1.59 suggesting higher electron density and thus a stronger C–Au bond. **f**, Calculated average mean square displacement of CO_2 on Au(111) surface with and without K^+ in the system. This ensemble average shows CO_2 is more diffuse without a K^+ cation to facilitate CO_2 surface binding. **g**, Mean square displacement of CO_2 on Au(111), Au(110), Au(100) and Au(211) surface in the presence of K^+. It was found that regardless of facet the mean square displacement of CO_2 converges to about 2.5 $Å^2$. **h**, Calculated C–Au radial distribution function under the conditions with or without K^+. The radial distribution function of CO_2 to Au(111) from an ensemble average of 25 *ab initio* molecular dynamics simulations (5 ps) shows CO_2 is closer to the surface of gold on average in the presence of K^+ than without K^+. **i**, Calculated interaction energy of CO_2 vary with C–Au distance under the conditions with or without K^+. The interaction energy is consistently less in the presence of an adsorbed K^+ (red) than without K^+ (black).

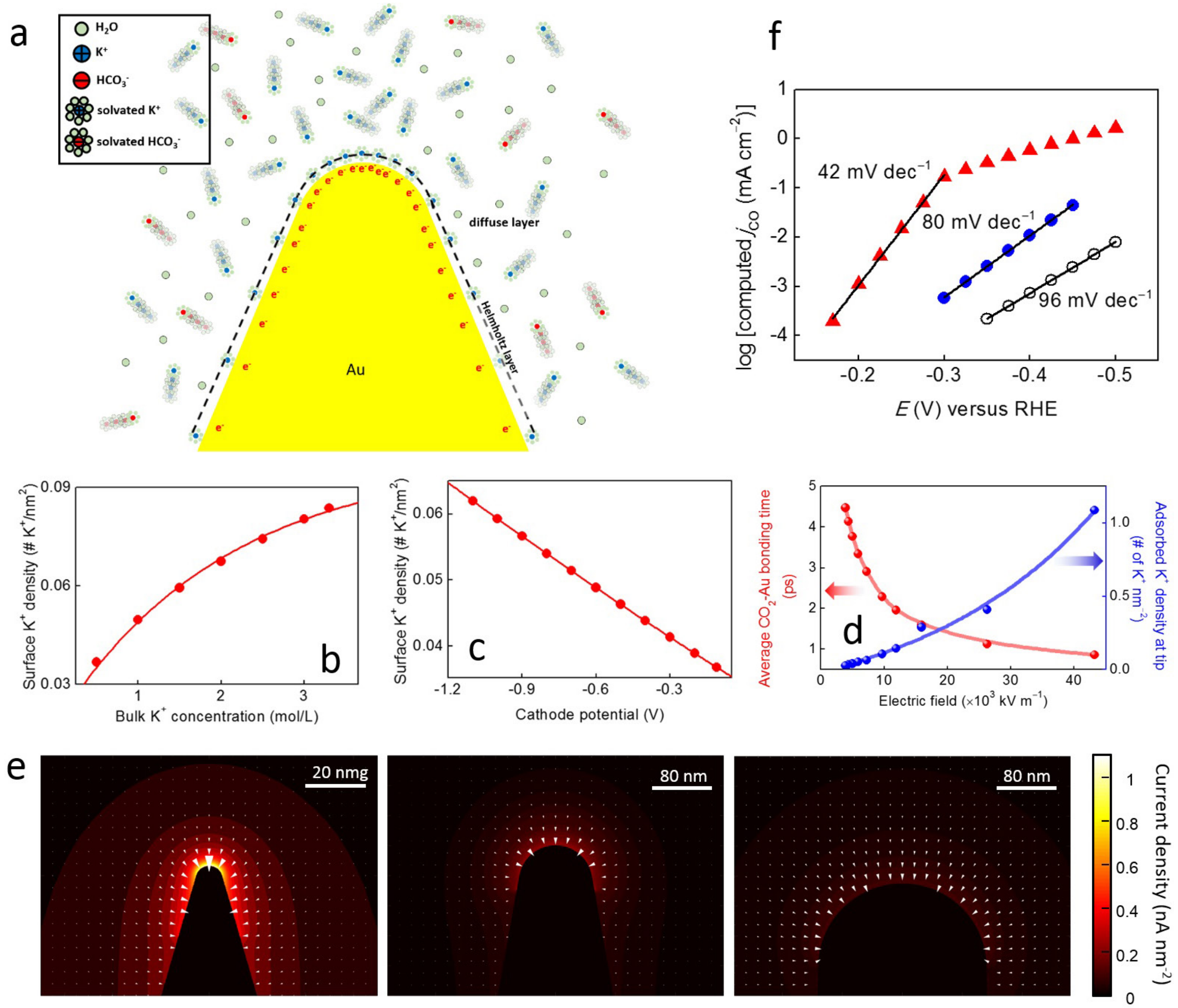

Extended Data Figure 2 | Electrochemical simulation model and results. a, Schematic of the Gouy–Chapman–Stern electrical double layer model. **b**, Field-induced surface K^+ ion concentration as a function of bulk K^+ ion concentration. **c**, Field-induced surface K^+ ion concentration as a function of electrode potential (versus RHE). **d**, Required CO_2–Au bonding time versus electric field. With concentrated K^+, CO_2 quickly (in 0.5 ps) stabilizes on the Au sharp features and remains there for the remainder of the simulation run. **e**, Current density distributions on the surface of Au structures. The tip radius is 5 nm. The tip radius of the structure in each panel is: 5 nm (top), 60 nm (middle) and 140 nm (bottom). Arrows are magnified 2× in the middle panel and 4× in the bottom panel for the purpose of clarity. **f**, Simulated Tafel plots for needles (tip radius 5 nm), rods (tip radius 60 nm), particles (tip radius 140 nm). Simulated data was fitted to the experimental data with fitting parameter cathodic charge transfer coefficient being 0.95 (needles), 0.49 (rods), and 0.43 (particles).

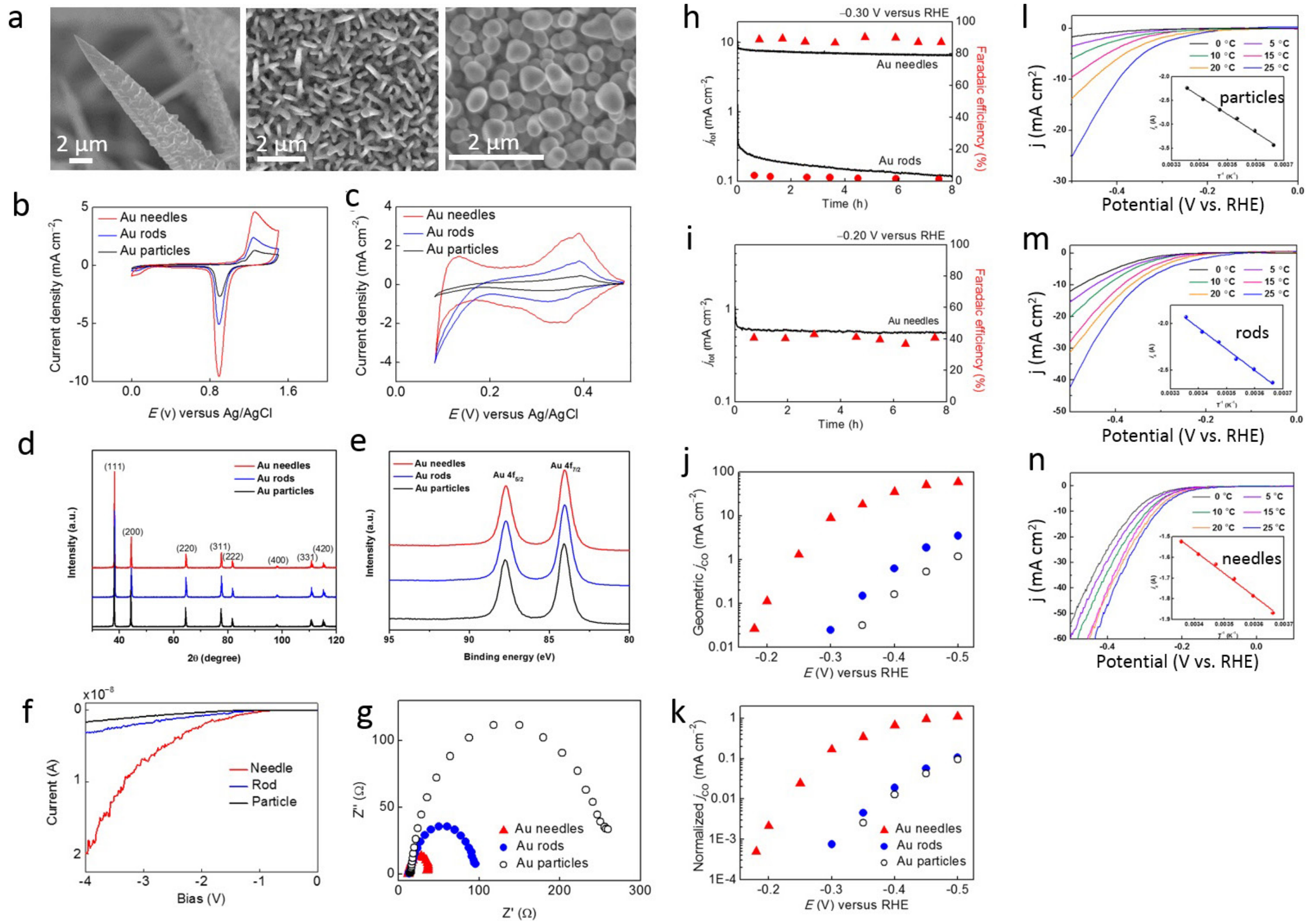

Extended Data Figure 3 | Additional physical characterization, CO_2 reduction and kinetic analyses of Au samples. a, Morphologies for Au tips (left), rods (middle) and particles (right) imaged by SEM. **b**, **c**, ECSA measurement. **b**, Cyclic voltammograms in 50 mM H_2SO_4. Scan rate 50 mV s^{-1}. **c**, Underpotential Cu deposition and anodic stripping waves. The electrolyte solution was 100 mM CuSO4 in 0.50 M H_2SO_4. Scan rate 50 mV s^{-1}. **d**, X-ray diffraction patterns for all of the electrodes exhibited peaks at the expected positions for an ideal Au lattice, indicating no uniform expansion or compression of the unit cell. **e**, X-ray photoelectron spectroscopy exhibited the expected peaks for Au^0 but no peaks attributable to an oxide, indicating that reduction of $HAuCl_4$ precursor was complete within the detection limits of this technique. **f**, Current–voltage curves on the tips of single Au needle, rod and particle. The radii for the Au needle, rod and particle are 5 nm, 60 nm and 140 nm, respectively. **g**, Charge transfer resistance analyses. Nyquist plots in 0.5 M $KHCO_3$ aqueous electrolyte. **h**, **i**, CO_2 reduction performances in 0.5 M $KHCO_3$, pH 7.2 at −0.30 V (**h**) and −0.20 V (**i**) versus RHE. **j**, **k**, CO_2 reduction current densities in 0.5 M $KHCO_3$, pH 7.2, normalized by (**j**) geometric area and (**k**) ECSA. **l**–**n**, Activation energy analyses. The polarization curves of Au particles (**l**), Au rods (**m**), and Au needles (**n**) in 0.5 M $KHCO_3$ aqueous electrolyte at 0–25 °C. Insets are the Arrhenius plots for the dependence of reaction rate for CO_2 reduction on temperature.

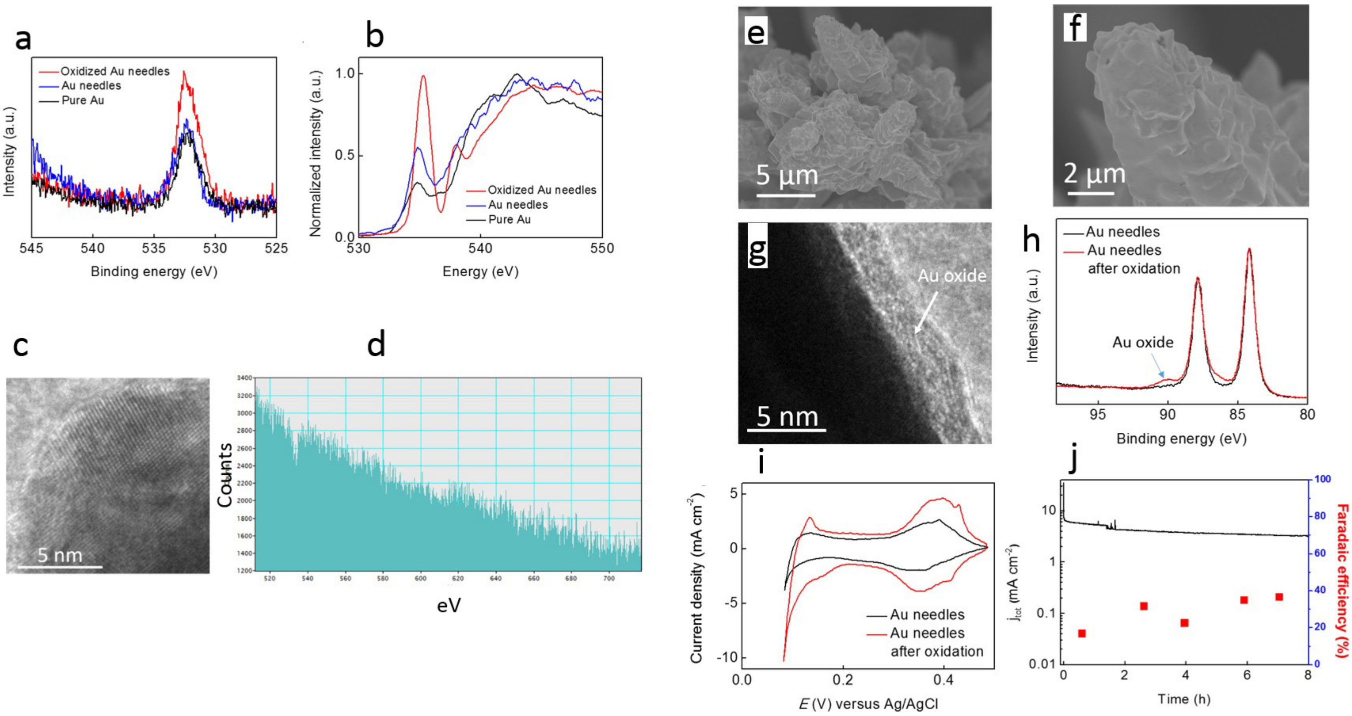

Extended Data Figure 4 | Collective control experiments to confirm that the reactivity of Au nanoneedles cannot be simply explained by oxides or adatoms. a, **b**, O 2*p* core-level X-ray photoelectron spectroscopy spectra (**a**) and O K-edge X-ray absorption spectra (**b**) for Au needles, pure Au and oxidized Au needles. The O 2*p* core-level and O K-edge X-ray absorption spectra of Au needles are similar to those of pure Au and are different from that of oxidized Au needles, indicating the different Au states in Au needles and oxidized Au. **c**, High-resolution TEM image of Au needle tip, indicating that there is no obvious facet and adatoms. **d**, Electron energy loss spectroscopy (EELS) spectra on Au needle tip. No oxide can be detected on Au needle tip, indicating that reduction of the $HAuCl_4$ precursor was complete within the detection limits of this technique. **e**, Low-magnification SEM image of oxidized Au needles. **f**, High-magnification SEM image of oxidized Au needles. **g**, TEM image of oxidized Au needles. Amorphous Au oxide can be observed on the surface of Au. **h**, X-ray photoelectron spectroscopy spectra of oxidized Au needles and primary Au needles. **i**, Cyclic voltammograms collected for Au needles, and oxidized Au needles. **j**, CO_2RR performance on oxidized Au needles.

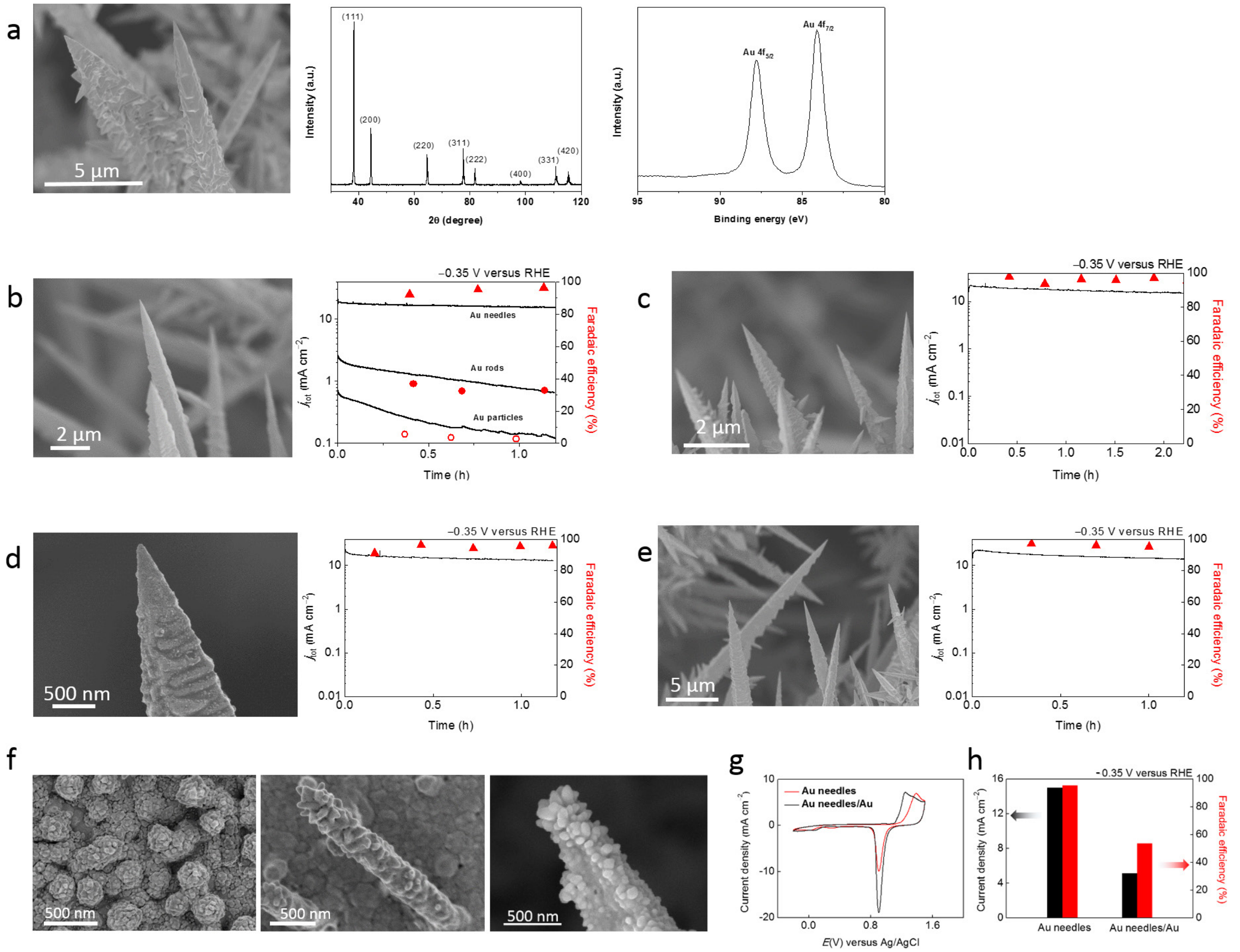

Extended Data Figure 5 | Collective control experiments to confirm the FIRC effects. a, Morphology, crystal structure and composition for Au needles after reaction. Left, SEM image, middle, X-ray diffraction pattern, and right, X-ray photoelectron spectroscopy spectrum for Au needles after long term CO_2RR. **b**, Left, SEM image of Au needles covered by 10-nm Au by electron bean deposition, right, CO_2 reduction activity of Au needles, rods and particles at −0.35 V versus RHE. **c**, Left, SEM image of Au needles at 140 °C after annealing, right, CO_2 reduction activity of Au needles at −0.35 V versus RHE after annealing. **d**, Left, SEM image of Au needles after surface etching. The Au nanoneedles were immersed in a vial containing 15 ml of $CuCl_2$ solution (5 mM). The vial was then heated to 70 °C using an oil bath and kept at that temperature for 1 h. The etched Au nanoneedles obtained were washed with a copious amount of water and dried at room temperature[27]. Right, CO_2 reduction activity of Au needles at −0.35 V versus RHE after surface etching. **e**, Left, SEM image of Au needles after surface plasma bombard (50 W, argon atmosphere, 1 h). Right, CO_2 reduction activity of Au needles at −0.35 V versus RHE after surface plasma bombard. **f**, SEM image of Au particles (left), Au rods (middle), and Au needles (right) with secondarily deposited Au particles. **g**, Cyclic voltammograms collected for Au needles in 50 mM H_2SO_4 for ECSA measurements. **h**, CO_2RR performances of Au needles and Au needles/Au at −0.35 V versus RHE.

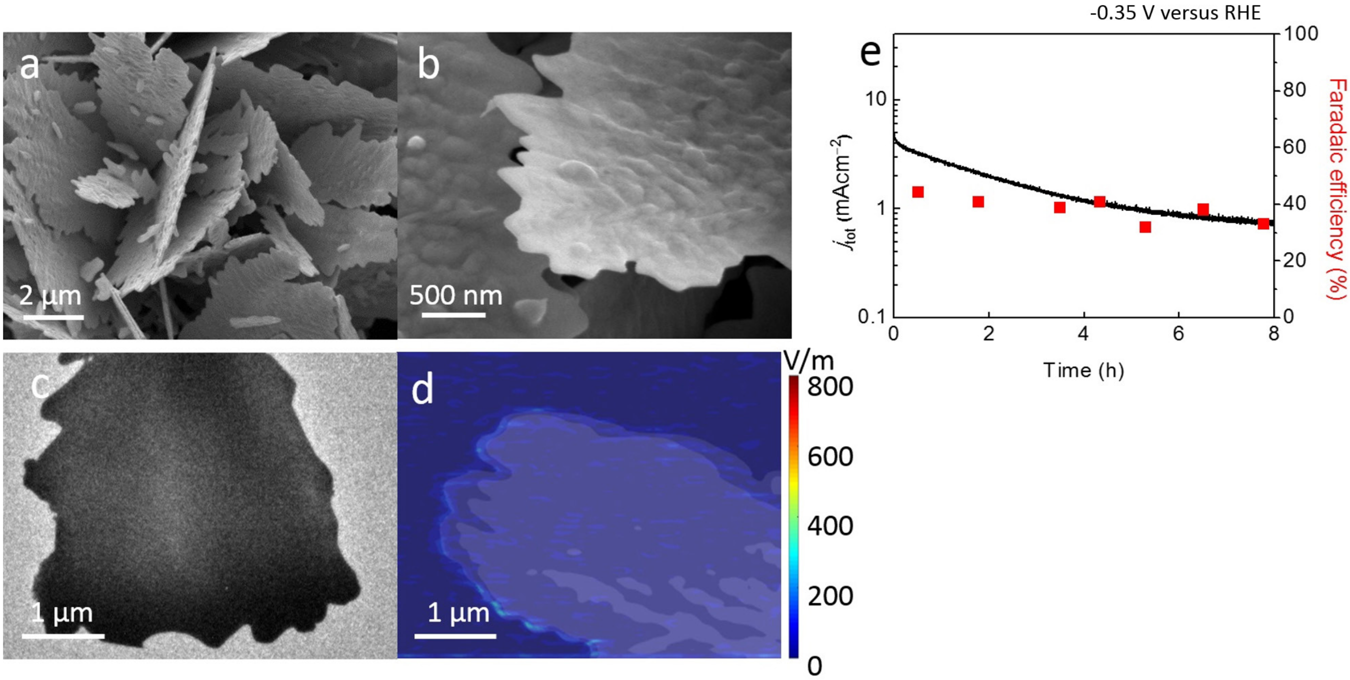

Extended Data Figure 6 | Morphology, electric field and CO_2 RR performance of dendritic Au leaves. **a**, **b**, SEM images of Au leaves. **c**, TEM image of Au leaves. **d**, Electric field distribution deduced using Kelvin probe atomic force microscopy. **e**, CO_2 reduction activity of Au leaves at −0.35 V versus RHE.

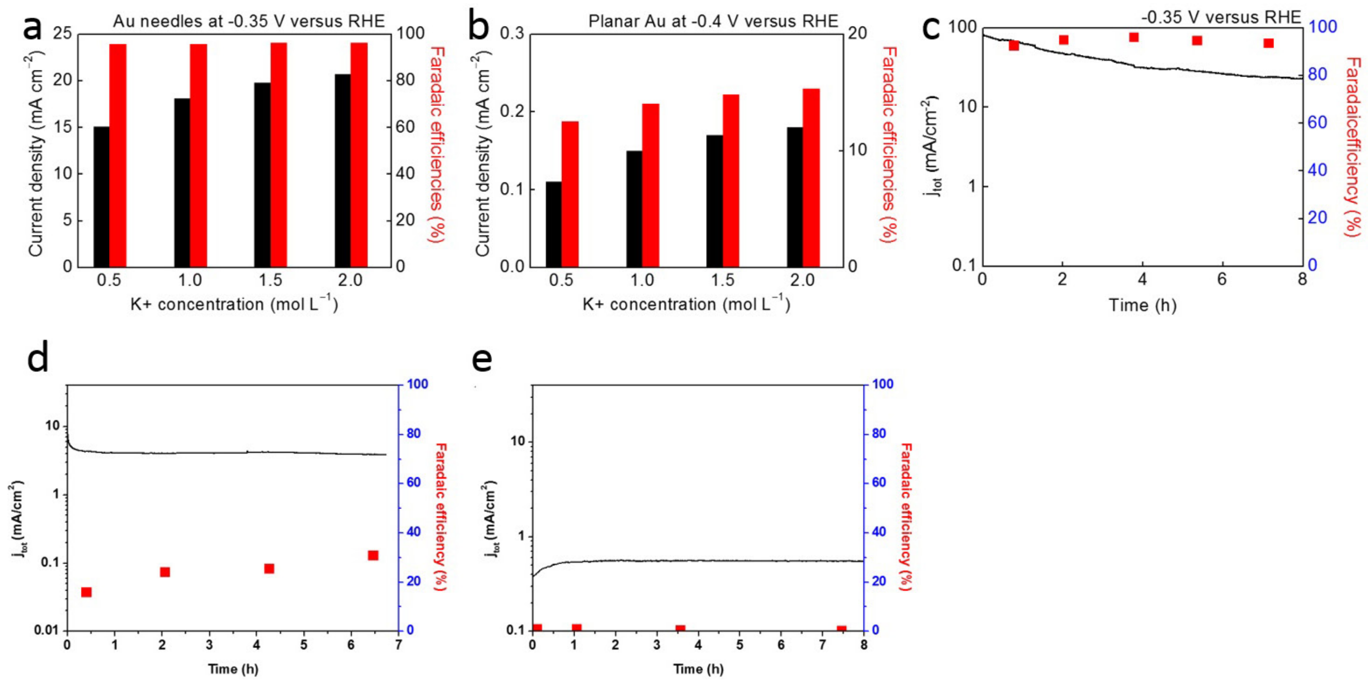

Extended Data Figure 7 | CO_2RR performances of Au nanoneedles in various electrolyte condition. **a**, Current densities and Faradaic efficiencies versus K^+ concentrations on Au needles at −0.35 V versus RHE. **b**, Current densities and Faradaic efficiencies versus K^+ concentrations on planar Au at −0.4 V versus RHE. **c**, CO_2 reduction performance of Au needles in saturated $KHCO_3$ solution. **d**, CO_2 reduction performance of Au needles in NH_4HCO_3 solution. **e**, CO_2 reduction performance of Au needles in water.

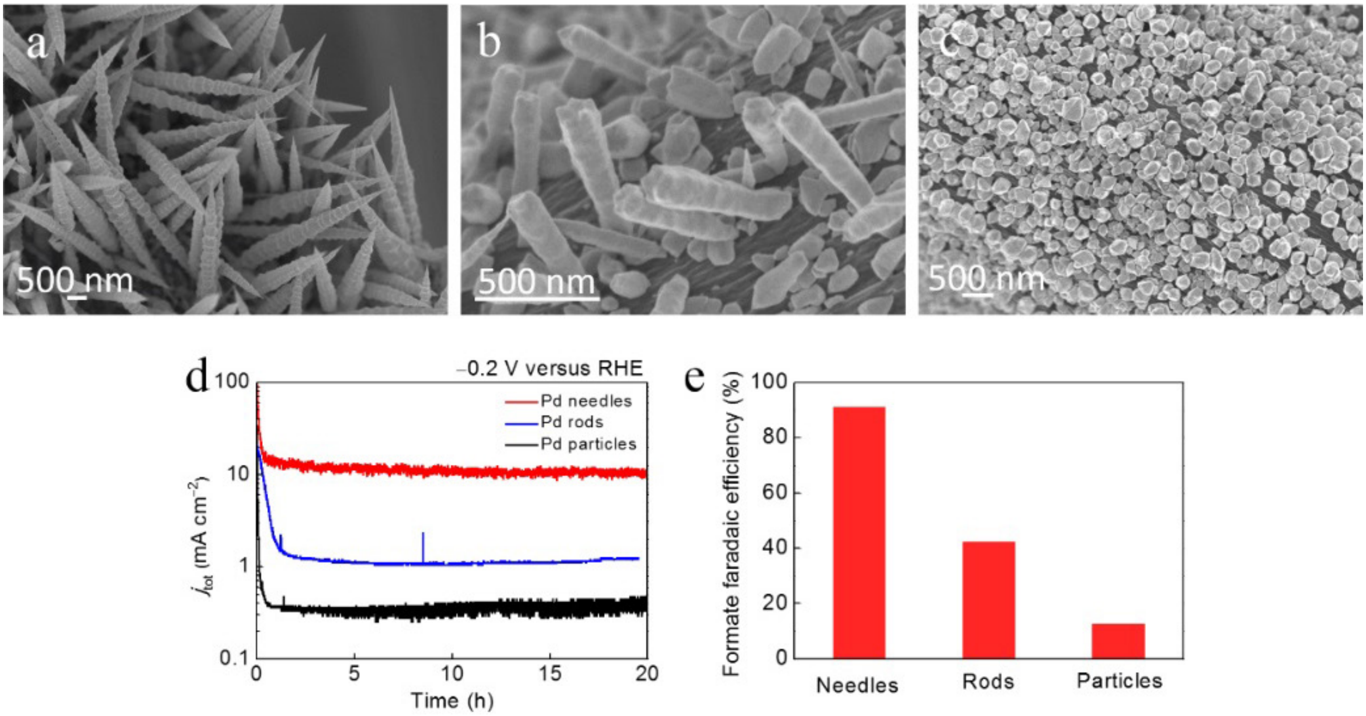

Extended Data Figure 8 | CO_2 reduction reaction performances on Pd needles, rods and particles. a–c, SEM images of Pd needles, rods and particles, respectively. **d**, Total current density versus time for CO_2 RR on Pd needles, rods and particles in 0.5 M $KHCO_3$ solution at −0.2 V versus RHE. **e**, Average Faradaic efficiency for formate production versus time on Pd needles, rods and particles in 0.5 M $KHCO_3$ solution at −0.2 V versus RHE.

Extended Data Table 1 | Summary of simulation parameters as calculated from DFT

A) Free Energy Corrections for gas-phase species (eV)

Species	E_{DFT}	ZPE	∫CvdT	TΔS	G
H_2O	-14.214	0.564	0.806	0.67	-14.218
CO_2	-22.946	0.306	0.099	0.662	-23.204
H_2	-6.771	0.268	0.091	0.434	-6.848
CO	-14.775	0.132	0.091	0.668	-15.221
HCOOH	-29.87	0.891	0.348	-1.047	-29.914

B) Free Energies for CO_2RR Reaction (eV)

Surface	Rxn Coordinate	ΔE			
		Au(111)	Au(100)	Au(110)	Au(211)
Bare	$CO_2 + * + 2(H^+ + e^-)$	0.00	0.00	0.00	0.00
	$COOH* + H^+ + e^-$	1.50	1.28	0.97	0.92
	$CO* + H_2O$	0.93	0.74	0.29	0.34
	$CO + * + H_2O$	0.61	0.61	0.61	0.61
K+	CO2 + * + 2(H+ + e-)	0.00	0.00	0.00	0.00
	COOH* + H+ + e-	0.61	0.61	0.28	0.40
	CO* + H2O	0.69	0.71	0.18	0.42
	CO + * + H2O	0.61	0.61	0.61	0.61

C) Free Energy Corrections for Surfaces and Adsorbates

Facet	Surface	Species	E_elec	ZPE	∫CvdT	TΔS	G
Au(111)	Bare	*	-81.61				
		CO*	-96.53	0.17	0.10	-0.25	-96.51
		COOH*	-107.27	0.65	0.09	-0.20	-106.73
	K+	*	-84.07				
		CO*	-99.26	0.17	0.09	-0.21	-99.21
		COOH*	-110.57	0.62	0.10	-0.24	-110.09
Au(100)	Bare	*	-79.01				
		CO*	-94.25	0.20	0.07	-0.13	-94.11
		COOH*	-104.88	0.64	0.10	-0.22	-104.37
	K+	*	-81.49				
		CO*	-96.72	0.18	0.08	-0.15	-96.61
		COOH*	-108.01	0.62	0.10	-0.22	-107.50
Au(110)	Bare	*	-103.85				
		CO*	-119.57	0.22	0.06	-0.10	-119.40
		COOH*	-130.13	0.67	0.08	-0.13	-129.51
	K+	*	-106.41				
		CO*	-122.24	0.22	0.06	-0.10	-122.06
		COOH*	-133.33	0.64	0.09	-0.16	-132.76
Au(211)	Bare	*	-80.61				
		CO*	-96.24	0.20	0.07	-0.13	-96.10
		COOH*	-106.87	0.65	0.09	-0.19	-106.32
	K+	*	-83.42				
		CO*	-98.93	0.18	0.08	-0.17	-98.84
		COOH*	-110.19	0.64	0.10	-0.19	-109.65

D) Average closest Au-CO_2 distance (Å)

Facet	Without K^+	With K^+	Facet	Without K^+	With K^+	Facet	Without K^+	With K^+	Facet	Without K^+	With K^+
(111)	3.25	2.75	(110)	3.24	2.75	(100)	3.28	2.79	(211)	3.29	2.80

ZPE, zero-point vibrational energy; $\int C_V dT$, heat capacity; T, temperature, ΔS, entropy; G, Gibbs energy.

Extended Data Table 2 | Summary of ECSA, activation energies and charge transfer resistances on different Au electrodes

Sample	Geometric area 1 (cm^2)	[a]ECSA 1 (cm^2)	Roughness factor 1	Geometric area 2 (cm^2)	[b]ECSA 2 (cm^2)	Roughness factor 2	[c]Activation energies (kJ mol^{-1})	[c]Charge transfer resistance (Ω)
Au needles	0.18	9.59	53.28	0.13	6.70	51.54	21	24
Au rods	0.21	6.91	32.90	0.23	7.86	34.17	44	92
Au particles	0.26	3.26	12.54	0.28	3.41	12.18	72	240

[a]ECSA 1, electrochemically active surface area, determined by integrating the oxide reduction peak area obtained from cyclic voltammogram.
[b]ECSA 2, electrochemically active surface area, determined by measuring anodic stripping waves for underpotential-deposited Cu monolayers.
[c]Measured in 0.5 M $KHCO_3$.

Extended Data Table 3 | Summary of CO_2RR performances on different Au and Pd electrodes in aqueous solution with inorganic electrolyte

Sample	Electrolyte	Product	Potential vs. RHE (mV)	$j_{product}$ (mA cm^{-2})	FE	Onset over-potential (mV)	Tafel slope (mV dec^{-1})	Reference
Au needles	0.5 M $KHCO_3$	CO	-350	~15	95%	70	42	This work
Au needles	[a]Sat. $KHCO_3$	CO	-350	~22	95%	70	–	This work
Au rods	0.5 M $KHCO_3$	CO	-350	~0.7	25%	190	80	This work
Au particles	0.5 M $KHCO_3$	CO	-350	~0.1	3%	240	96	This work
Oxide-derived Au	0.5M $NaHCO_3$	CO	-350	~2	96%	140	56	Reference *(9)*
Au nanowire	0.5 M $KHCO_3$	CO	-350	~1.8[b]	94%	90	–	Reference *(25)*
Au NP's	0.5 M $NaHCO_3$	CO	-350	<0.02	63%	190	–	Reference *(24)*
Pd needles	0.5 M $KHCO_3$	HCOOH	-200	~10	91%	–	–	This work
Pd rods	0.5 M$KHCO_3$	HCOOH	-200	~0.5	42%	–	–	This work
Pd particles	0.5 M $KHCO_3$	HCOOH	-200	~0.05	13%	–	–	This work
Partially oxidized Co	0.1 M Na_2SO_4	HCOOH	-200	~3	45%	–	–	Reference *(2)*
Pd NP's	0.5 M $KHCO_3$	HCOOH	-200	~1	50%	–	–	Reference *(28)*
Pd NP's	2.8 M $NaHCO_3$	HCOOH	-200	~0.4	82%	–	–	Reference *(28)*

[a]Sat. $KHCO_3$, saturated $KHCO_3$ solution.
[b]The unit of current density is A g^{-1}.
Data is taken from refs 2, 9, 24, 25 and 28. NP, nanoparticle; FE, Faradaic efficiency.